LAWRENCE
LIVERMORE
NATIONAL
LABORATORY

LLNL-JRNL-456333

Measurements of Core and Compressed Shell Temperature and Density Conditions in Thick-Wall Target Implosions at OMEGA

R. Florido, R. C. Mancini, T. Nagayama, R. Tommasini, J. A. Delettrez, S. P. Regan, B. Yaakobi

September 21, 2010

Physical Review Letters

Disclaimer

Measurements of Core and Compressed Shell Temperature and Density Conditions in Thick-Wall Target Implosions at OMEGA

R. Florido,[1,*] R. C. Mancini,[1] T. Nagayama,[1] R. Tommasini,[2] J. A. Delettrez,[3] S. P. Regan,[3] and B. Yaakobi[3]

[1] *Department of Physics, University of Nevada, Reno, NV 89557, USA*
[2] *Lawrence Livermore National Laboratory, Livermore, CA 94550, USA*
[3] *Laboratory for Laser Energetics, University of Rochester, Rochester, NY 14623, USA*

(Dated: July 23, 2010)

A spectroscopic method is discussed to measure core and compressed shell conditions in thick-wall plastic-shell implosions at OMEGA filled with deuterium and a tracer amount of argon. A spectrometer was used to record x-ray spectra with high-resolution over a broad wavelength range. The simultaneous observation of argon line emission and the attenuation and self-emission effects of the compressed shell confining the core yielded enough information to extract temperature and density conditions in both core and compressed shell.

PACS numbers: 32.30.Rj, 52.25.Os, 52.57.-z, 52.70.La

The idea of inertial confinement fusion (ICF) is to compress a few miligrams of fuel to temperatures and densities high enough for thermonuclear fusion to proceed while mass inertia keeps the burning fuel assembled. The required core temperature and density conditions are achieved by imploding spherical shells driven by an intense energy pulse usually delivered by laser beams [1]. Knowledge of these conditions is critical to understand the implosion's hydrodynamics. In this regard, x-ray spectroscopy has proved to be a powerful method to diagnose core conditions at the implosion collapse [2]. Here, we discuss a novel spectroscopic method for the simultaneous diagnosis of both core and compressed shell, and areal-density conditions in thick-wall target implosions, such as those employed in recent shock ignition ICF experiments [3, 4]. It relies on the idea that a broad-band spectroscopic measurement with sufficient spectral resolution can be used to extract information from several regions of a high-energy density system. In particular, for thick-wall shock ignition implosions it employs the analysis of a tracer's x-ray spectrum over a broad range of wavelengths including line features emitted in the core, and attenuation due to and continuum self-emission from the compressed shell.

The shock ignition implosions discussed here employed plastic shell targets that had an internal radius of 387 μm, a plastic wall thickness of 40 μm, and an outer aluminum coating of 0.1 μm for sealing purposes. They were filled with 20 atm of D_2 and 0.072 atm of Ar, which was used for spectroscopic diagnosis. The capsules were irradiated by a low-adiabat pulse shape of ~18.6 kJ UV laser energy on target comprised of a 80 ps FWHM picket, followed by a 1.5 ns long main drive with a sharp intensity spike at the end in order to launch the ignitor shock wave. The observed argon radiation emission includes K-shell x-ray line transitions that span the photon energy range from 3000 eV to 4400 eV. An absolutely calibrated x-ray flat crystal spectrometer with a spectral resolution power of $\lambda/\Delta\lambda \approx 1200$ was used to obtain time- and space-integrated x-ray line spectra from the argon tracer.

An example of a time- and space-integrated spectrum recorded in the experiments is displayed in Fig. 1. This emission is characteristic of a time interval of approximately 250 ps at the collapse of the implosion. Line transitions in He- and H-like Ar ions are observed and labeled in the spectra, namely Heα $1s^2$-1s2p, Lyα 1s-2p, Heβ $1s^2$-1s3p, Heγ $1s^2$-1s4p, Lyβ 1s-3p, and Lyγ 1s-4p. Weaker, and sometimes heavily blended with parent lines, satellite line transitions arising from autoionizing states in He- and Li-like Ar ions are also present in the data. The spectrum is significantly attenuated at low photon energies. This attenuation is so severe that the usually strong Heα and Lyα lines appear among the weakest emission lines in the spectrum. This effect is interpreted in terms of the radiation absorption that takes place in the compressed shell confining the core, due to inverse bremsstrahlung (free-free) and photoionization (bound-free) processes.

The model used to analyze the data is schematically illustrated in Fig. 2. It consists of a uniform sphere to characterize the state of the implosion core surrounded by a uniform concentric shell to account for the compressed shell confining the core. The parameters of the model are the core radius R, electron temperature T_c and electron density N_c, and the compressed shell thickness

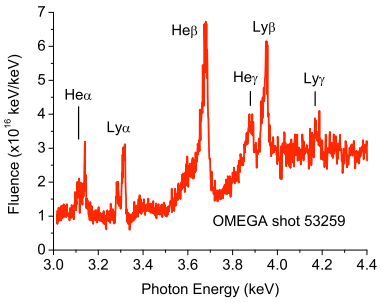

FIG. 1. Space- and time-integrated spectrum for thick-wall target shock ignition implosion.

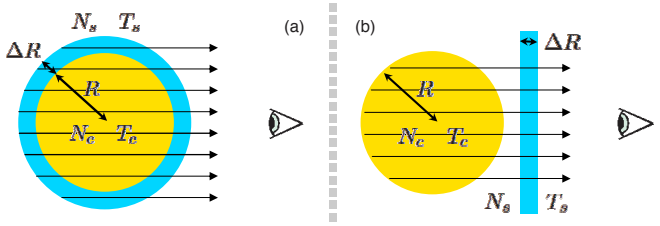

FIG. 2. (a) Schematic illustration of the model used to analyze the data, (b) Simpler geometry with analytical solution.

ΔR, electron temperature T_s and electron density N_s. On the one hand, the value of R can be computed from N_c assuming mass conservation; we note in passing that this assumption relies on the approximation that all of the core mass contributes to the emission of radiation. On the other hand, the value ΔR is calculated from the values of R and N_s, as well as the fraction α of shell mass that is imploded. The uniform model approximation for the spherical shell requires that the same imploded shell mass that contributes to the attenuation of the core radiation also contributes to the self-emission of the shell. The value of α is estimated from LILAC 1D [5] hydrodynamic simulations of the implosion. Thus, the model depends actually on four parameters: T_c, N_c, T_s and N_s. To calculate the emergent intensity distribution for this model, we integrate the radiation transport equation for each photon energy along chords parallel to the direction of observation, and then further integrate all individual chord contributions to obtain the space-integrated spectrum for comparison with the experimental spectrum. Before comparing with data, the synthetic spectrum is convolved with the instrumental function to account for the finite spectral resolution of the instrument.

The frequency-dependent emissivity and opacity of the core and shell were calculated with population number densities from the collisional-radiative atomic kinetics model ABAKO [6]. All bound-bound, bound-free and free-free contributions from the argon-deuterium plasma in the core, and the carbon-hydrogen plasma in the compressed shell within the spectral range of the measurements were included. Energy levels and line transition rates were computed using the atomic structure code FAC [7]. For a given set of plasma temperature and density conditions, ABAKO takes into account all non-autoionizing and autoionizing states consistent with the continuum-lowering, which is estimated according to the Stewart and Pyatt model [8]. Continuum lowering is particularly important for determining the ionization balance of the compressed shell and thus the contributions of photoionization and inverse bremsstrahlung to the total opacity of the compressed shell. Radiation transport effects on level population kinetics were considered via escape factors [9], and detailed Stark-broadened line shapes were used for parent and satellite transitions of the argon spectrum [10]. For completeness, natural and Doppler line broadening were included as well. For data analysis, the model geometry of Fig. 2(a) was used. However, to gain insight into the model characteristics and the dependence on model parameters, a simplified model geometry is shown in Fig. 2(b) which corresponds to the case of a spherical plasma source (core) seen through a plasma slab (shell). The advantage of this simplified model geometry is that it has the same underlying physics of the model in Fig. 2(a) but the radiation transport equation can be integrated analytically, namely,

$$F^\nu = \pi R^2 \frac{\varepsilon_c^\nu}{\kappa_c^\nu}\left[1+\frac{e^{-2\kappa_c^\nu R}}{\kappa_c^\nu R}-\frac{\left(1-e^{-2\kappa_c^\nu R}\right)}{2(\kappa_c^\nu R)^2}\right]e^{-\kappa_s^\nu \Delta R}+ \pi R^2 \frac{\varepsilon_s^\nu}{\kappa_s^\nu}\left(1-e^{-\kappa_s^\nu \Delta R}\right), \quad (1)$$

where F^ν is the emergent intensity distribution, and ε_c^ν, κ_c^ν, ε_s^ν and κ_s^ν stand for the temperature, density and photon energy dependent emissivity and opacity of the core and the shell, respectively. The first term in Eq. (1) represents the radiation emitted by the core further attenuated by the transmission through the shell, and the second one represents the self-emission of the shell. Fitting the observed spectrum to the model by means of a weighted least-squares minimization procedure yields both core and shell temperature and density conditions. Furthermore, from N_c, R, N_s and ΔR the areal density ρR of the imploded target can also be obtained. To determine the best fit parameters and check their uniqueness, we performed exhaustive searches in parameter space for a given value of α. This is also important in order to test the model sensitivity on the T_c, N_c, T_s and N_s parameters. The T_c and N_c dependence is mainly determined by the argon line emission. The argon K-shell spectrum is sensitive to plasma electron temperature and density conditions through the temperature and density sensitivity of the atomic level population kinetics and the density dependence of the Stark-broadened line shapes. The dependence on N_s and T_s is brought about by the shell opacity that attenuates the emission of the core as it goes through the compressed shell. There is also T_s sensitivity in the continuum of the shell self-emission that becomes significant in the low photon energy end of the spectrum, i.e. the slope of the underlying continuum is dependent on T_s. The overall attenuation effect of the spectrum depends also on the areal density of the compressed shell, which in turn depends on N_s and ΔR. We note that an attenuation effect for thick wall targets due to a high areal density shell was previously observed but only on broad band continuum emission measurements [11]. In this work, the attenuation effect is also observed on the line emission from the dopant in the core. Hence, both line and continuum emission and attenuation have to be modeled simultaneously and self-consistently to produce a good approximation to the data.

In order to test the method, we first apply it to the

analysis of several synthetic data test cases. To this end, the 1D hydrodynamics code LILAC was used to simulate a shock ignition implosion with the same characteristics of the experiments performed at OMEGA. Then, the time-history of temperature and density spatial profiles computed by LILAC were post-processed with the same atomic kinetics model used in the data analysis, to compute the emergent space-integrated and either time-resolved or time-integrated spectra. We emphasize that the spectroscopic analysis can be applied to either time-resolved or time-integrated spectra. The results of the analysis of synthetic spectra are illustrated in Fig. 3. Plots labeled (a), (b), and (c) show the comparison of three time-resolved synthetic spectra separated 60 ps between each other in time before stagnation, and best model fits. As seen in Fig. 3 good agreement was found for all cases. Since both LILAC simulations and the spectroscopic model assume spherical symmetry, differences between model fit and LILAC post-processed spectra can be attributed to the non-uniform temperature and density spatial profiles from the hydro simulation. The conditions extracted from the analysis are T_c = 1050, 1050 and 965 eV; N_c = 1.1×10^{24}, 2.0×10^{24} and 4.0×10^{24} cm^{-3}; T_s = 240, 295 and 310 eV; and N_s = 8.7×10^{24}, 1.1×10^{25} and 1.2×10^{25} cm^{-3} for (a), (b) and (c), respectively. These values fall within the range of values of the simulation spatial profiles. We verified that for all cases the searches in parameter space yielded a single, global minimum. However, we note that if T_s is lower than ∼200 eV the sensitivity on T_s is significantly lost and the results for T_s and N_s become ambiguous. For the areal densities we get ρR= 0.12, 0.16 and 0.20 gcm^{-2} which compare well with the simulation values of 0.10, 0.14 and 0.18 gcm^{-2}. Fig. 3(d) shows the analysis of the synthetic space- and time-integrated spectrum, i.e. the synthetic spectrum equivalent to the spectrum recorded in the experiment. For this case, similar differences are observed between model fit and post-processed spectra but overall the approximation is still good. The analysis of this case also yields values that compare well with the hydrodynamic simulation, namely T_c = 965 eV, N_c = 1.8 × 10^{24} cm^{-3}, T_s = 305 eV, N_s = 1.2 × 10^{25} cm^{-3}, and ρR = 0.16 gcm^{-2}.

Next, we analyze the space- and time-integrated experimental spectrum. The result is displayed in Fig. 4, which shows the comparison between experimental and best model fit spectra. The experimental spectrum plotted in Fig. 4 is an average of data recorded in two nominally identical OMEGA shots, i.e. 53258 and 53259, that were done to check reproducibility. The benefit of the average is that it improves the signal-to-noise ratio. Also shown in Fig. 4 is the time-integrated synthetic spectrum from LILAC post-processing of Fig. 3. The synthetic, post-processed spectrum shows a smaller amount of attenuation of the α lines compared to the experiment, and a smaller underestimation of the data in the region between Lyα and Heβ, and Heβ and Lyβ lines. The latter suggests that non-uniformities are, in part, responsible for this difference with the best model fit but cannot explain all of it. We emphasize that the exhaustive search in parameter space for the best model fit yielded a single, global minimum characterized by a value of the normalized, weighted $\chi^2 \sim 1$. The uncertainties in the spectrum data points were estimated from the spread in the data. The comparison shows disagreements for photon energies between Lyα and Heβ, and also between Heβ and Lyβ lines where the model fit significantly underestimates the experimental intensity. Accordingly, these portions of the spectrum were not included in the χ^2 calculation. These differences are interpreted, in principle, as due to line emissions from satellite transitions in lower ionization states of Ar in low temperature regions of the core that cannot be accounted for in a uniform plasma approximation, and deviations from spherical symmetry; in fact, three-dimensional effects are observed in x-ray images of the implosion core. Overall, the intensity distribution of the argon line emission, including the attenuation through the shell, is well described by the model over a photon energy range of 1.4 keV. We note that the effect of the continuum self-emission of the shell is visible in the low photon energy end of the spectrum. Thus, the model incorporates the essential physics to describe the core emission and the strong absorption in the denser and colder shell surrounding the imploded core, that results in a significant attenuation of the Heα-Lyα lines relative to the Heβ-Lyγ lines region.

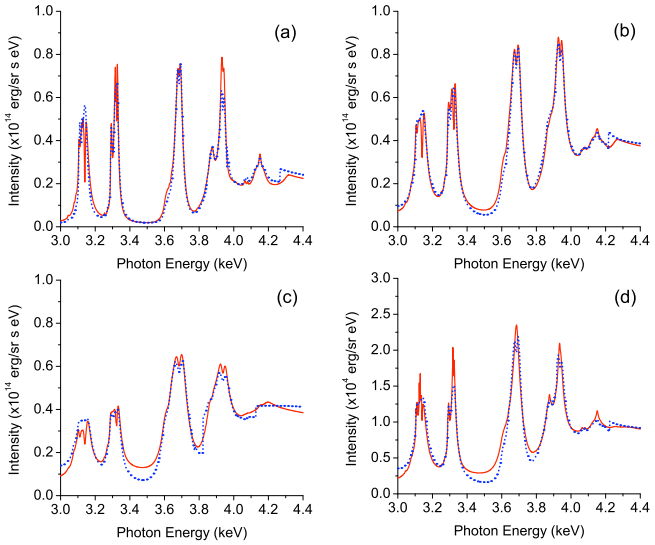

FIG. 3. Spectroscopic analysis of synthetic data from post-processed hydrodynamic simulation: (solid red) synthetic spectra, (dotted blue) best model fit.

The values extracted from the analysis were T_c = 930 eV ± 5%, N_c = 1.0 × 10^{24} cm^{-3} ± 20%, T_s = 285 eV ± 6%, N_s = 3.8 × 10^{25} cm^{-3} ± 25%, and ρR =

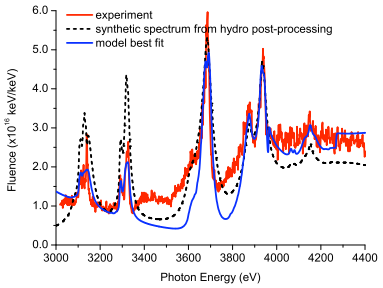

FIG. 4. Comparison of experimental, post-processed and best model fit spectra.

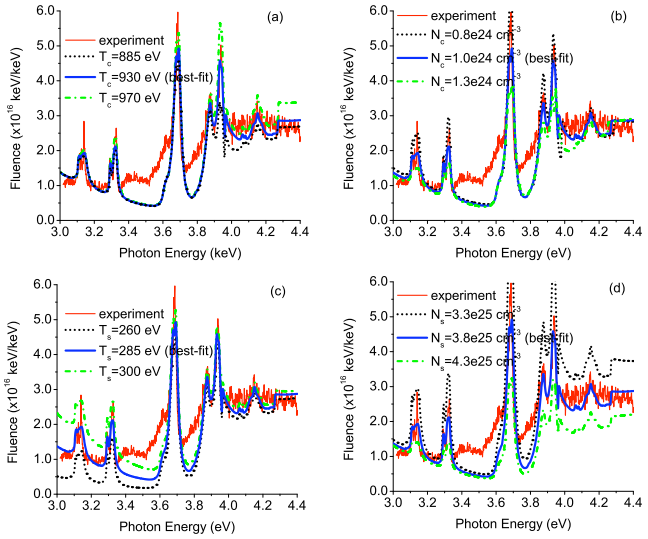

FIG. 5. Model spectrum sensitivity to changes in each of the four fitting parameters: (a) T_c, (b) N_c, (c) T_s, (d) N_s.

0.17 gcm$^{-2} \pm 20\%$. The uncertainties in the parameters were calculated by means of an analysis of the curvature of the four-dimensional weighted-χ^2 surface about the minimum, taking into account the correlations between the parameters [12]. We note that the compressed shell density N_s extracted from the experimental spectrum analysis is about three times larger than that from the post-processed spectrum while both areal-density values are comparable. This indicates that in the LILAC simulation the compressed shell is less dense but extends over a larger spatial region compared to the experiment. The larger density observed in the experiment results in a mass absorption coefficient (which for these conditions is dominated by free-free absorption) that is about two times larger than for the conditions in the LILAC simulation of the compressed shell. In turn, this results in the larger attenuation effect observed in the experiment. Since the diagnosis of the core and shell conditions relies on the sensitivity of the emergent intensity distribution on the model parameters, we illustrate this dependence in the sequence of plots Fig. 5(a)-(d). Each plot shows the change of the spectrum due to the variation of one parameter by increasing and decreasing its value within its uncertainty range. It is important to note that the change of each parameter causes a characteristic change in the spectrum. Four parameters are needed to accommodate the entire spectrum, and there is enough information to uniquely determine the core and shell temperature and density conditions. We note in closing that initial thick-wall shock ignition experiments performed at OMEGA [4] reported areal density values, inferred from the analysis of the energy distribution of secondary protons, of ~ 0.18 gcm^{-2} and ~ 0.16 gcm^{-2} for optimized and non-optimized spike pulse shapes, respectively, and using undoped targets filled with 25 atm of D_2. The spectroscopic analysis of the shock ignition experiments discussed here produced areal density values consistent with the results of those early experiments based on particle diagnostics. However, the spectroscopic analysis also yielded the temperature and density conditions of the core and compressed shell which are important characteristics of the fuel assembly at the collapse of the implosion, thus providing a more complete picture of the final conditions achieved in the shock ignition experiment.

This work was supported by DOE/NLUF Grant DE-FG52-09NA29042 and LLNL. R. Florido has also been supported by Spanish Ministry of Science and Innovation Grant No. ENE2008-06668-C02/FTN and the *Keep-in-Touch* Project of the EU. Prepared by LLNL under Contract DE-AC52-07NA27344.

* Permanent address: Departamento de Física, Universidad de Las Palmas de Gran Canaria, 35017 Las Palmas de Gran Canaria, Spain

[1] S. Atzeni and J. Meyer-Ter-Vehn, *The Physics of Inertial Fusion* (Oxford University Press, 2004).
[2] C. J. Keane *et al.* Phys. Rev. Lett., **72**, 3029 (1994); D. A. Haynes *et al.* Phys. Rev. E, **53**, 1042 (1996); N. C. Woolsey *et al.* *ibid.*, **56**, 2314 (1997); J. E. Bailey *et al.* Phys. Rev. Letters, **92**, 085002 (2004).
[3] R. Betti *et al.* Phys. Rev. Lett., **98**, 155001 (2007).
[4] W. Theobald *et al.* Phys. Plasmas, **15**, 056306 (2008).
[5] J. Delettrez *et al.* Phys. Rev. A, **36**, 3926 (1987).
[6] R. Florido *et al.* Phys. Rev. E, **80**, 056402 (2009).
[7] M. F. Gu, Can. J. Phys., **86**, 675 (2008).
[8] J. C. Stewart and K. D. Pyatt, Astrophys. J., **144**, 1203 (1966).
[9] R. C. Mancini, R. F. Joyce, and C. F. Hooper, Jr., J. Phys. B: At. Mol. Phys., **20**, 2975 (1987).
[10] R. C. Mancini *et al.* Comput. Phys. Commun., **63**, 314 (1991).
[11] B. Yaakobi, R. Epstein, and F. J. Marshall, Phys. Rev. A, **44**, 8429 (1991); F. J. Marshall *et al.* Phys. Rev. E, **49**, 4381 (1994).
[12] *Numerical Recipes: The Art of Scientific Computing*, 3rd ed. (Cambridge University Press, 2007).